

High-performance bilayer IGZO thin-film transistors by sputtering heterojunction with differences in indium elemental content

Longfei Zhang(张龙飞), Hanzhe Zhang(张翰哲), Yuhang Wang(王宇航), Shichen Su(宿世臣), Xianghu Wang(王相虎), Dezhen Shen(申德振), and Hai Zhu(朱海)

Citation: Chin. Phys. B, 2025, 34 (**10**): 108101. DOI: 10.1088/1674-1056/add67d
http://cpb.iphy.ac.cn; http://iopscience.iop.org/cpb

What follows is a list of articles you may be interested in

Pressure-induced metallization and Lifshitz transition in quasi-one-dimensional $TiSe_3$ single crystal

Zhenhai Yu(于振海), Yunguan Ye(叶运观), Pengtao Yang(杨芃焘), Yiming Wang(王弈铭), Liucheng Chen(陈刘城), Chenglin Li(李承霖), Jian Yuan(袁健), Ziyi Liu(刘子儀), Zhiwei Shen(申志伟), Shaojie Wang(王邵杰), Mingtao Li(李明涛), Chaoyang Chu(楚朝阳), Xia Wang(王霞), Jun Li(李俊), Lin Wang(王霖), Wenge Yang(杨文革), and Yanfeng Guo(郭艳峰)

Chin. Phys. B, 2025, 34 (**8**): 088102. DOI: 10.1088/1674-1056/adce9d

Spatial electron tunneling leads to space-charge-limited current in organic hole transport materials

Shaofeng Chen(陈绍枫), Yanfei Lu(鲁燕飞), Dongcheng Chen(陈东成), and Shi-Jian Su(苏仕健)

Chin. Phys. B, 2025, 34 (**7**): 078101. DOI: 10.1088/1674-1056/adcb1d

Two-step growth of 4-inch multilayer MoS_2 wafers

Yang-Kun Zhang(张养坤), Yu-Chen Wang(王雨辰), Wei Yang(杨威), Dong-Xia Shi(时东霞), Luo-Jun Du(杜罗军), and Guang-Yu Zhang(张广宇)

Chin. Phys. B, 2025, 34 (**6**): 068103. DOI: 10.1088/1674-1056/adce9f

Single crystal growth and transport properties of narrow-bandgap semiconductor RhP_2

De-Sheng Wu(吴德胜), Ping Zheng(郑萍), and Jian-Lin Luo(雒建林)

Chin. Phys. B, 2024, 33 (**8**): 088101. DOI: 10.1088/1674-1056/ad4cd5

Regulating the dopant clustering in LiZnAs-based diluted magnetic semiconductor

Zihang Jia(贾子航), Bo Zhou(周波), Zhenyi Jiang(姜振益), and Xiaodong Zhang(张小东)

Chin. Phys. B, 2024, 33 (**5**): 058101. DOI: 10.1088/1674-1056/ad3034

High-performance bilayer IGZO thin-film transistors by sputtering heterojunction with differences in indium elemental content

Longfei Zhang(张龙飞)[1], Hanzhe Zhang(张翰哲)[2], Yuhang Wang(王宇航)[2], Shichen Su(宿世臣)[2,†], Xianghu Wang(王相虎)[3,‡], Dezhen Shen(申德振)[4], and Hai Zhu(朱海)[1,§]

[1] *State Key Laboratory of Optoelectronic Materials and Technologies, School of Physics, Sun Yat-Sen University, Guangzhou* 510275, *China*
[2] *Institute of Semiconductor Science and Technology, South China Normal University, Foshan* 528225, *China*
[3] *School of Materials, Shanghai Dianji University, Shanghai* 200245, *China*
[4] *Gusu Laboratory of Materials, Suzhou* 215031, *China*

(Received 2 April 2025; revised manuscript received 7 May 2025; accepted manuscript online 9 May 2025)

The high-quality semiconductor InGaZnO (IGZO) alloy thin films with different indium (In) elemental contents were deposit utilized magnetron sputtering. The novel bilayer heterojunction TFT devices based on our fabricated IGZO films were proposed, and their performance exhibited significant improvement compared to single layer IGZO TFTs. In the bilayer heterojunction TFT, the field-effect mobility was promoted to 23.5 $cm^2 \cdot V^{-1} \cdot s^{-1}$, the switching ratio reached 4.1×10^7, and the subthreshold swing was reduced to 0.42 V/dec. Moreover, the variation of bilayer TFTs threshold voltage (V_{th}) was significantly suppressed, Under positive gate bias stress (PBS) and negative gate bias stress (NBS), the threshold shift is reduced to be 1.5 V and −1.1 V, respectively. The heterojunction within the bilayer IGZO films constructs a potential barrier at the interface, which facilitated the accumulation of channel electrons. Additionally, the low In-element content passivation layer in IGZO films not only preserved the channel of TFT but also reduced electron scattering, thereby the performance properties of TFT were enhancing. The excellent transistor characteristics of devices demonstrate the feasibility of our proposed bilayer heterojunction TFT, which will promote the basic research of IGZO device and accelerate the practical application of transparency IGZO TFT.

Keywords: semiconductor, alloy film, field effect, transistors

PACS: 81.05.Gc, 85.30.Tv, 61.43.Dq, 71.20.Nr

DOI: 10.1088/1674-1056/add67d **CSTR:** 32038.14.CPB.add67d

1. Introduction

The semiconductor thin-film transistors (TFTs) play a pivotal role in the realm of large-area electronic devices and serve as indispensable components in active matrix displays.[1] With the growing demand for high-resolution displays, the conventional amorphous silicon (a-Si) TFTs are no longer able to meet the requirements due to their low mobility.[2] Although polycrystalline silicon TFTs exhibit high mobility, they are burdened with high costs and poor uniformity during the preparation process. In contrast, metal oxide thin-film transistors have emerged as a highly promising alternative, boasting exceptional performance characteristics such as high mobility, excellent optical transparency, and low process temperature. Moreover, their production cost remains relatively reasonable, which has led to widespread attention from both industrial and academic sectors.[3–5] Notably, amorphous indium gallium zinc oxide (a-IGZO) TFTs have gained prominence as the first commercially viable metal–oxide material for TFTs. This is attributed to their elevated mobility, large-area uniformity, steep subthreshold swing, and compatibility with conventional complementary metal–oxide semiconductor (CMOS) technology.[6] Actually, a-IGZO TFTs have been extensive applied in liquid crystal displays, flexible electronic, devices organic light-emitting diodes, and image sensors.[1,6–13]

However, the further promotion of both high mobility and high stability for a-IGZO TFTs confront the significant challenge. Therefore, various approaches have been explored in recent years, including elemental doping, plasma treatment, and the double-gate structures. For instance, doping of magnesium (Mg) during the sputtering process of IGZO has been investigated.[14] The treatments involving H_2, N_2/H_2, Ar/O_2, and N_2O plasma have been employed for the fabrication of IGZO films.[15–17] Additionally, the introduction of dual SiO_x insulating layer, dual gate structure, low temperature SiO_2/Si_3N_4 passivation layer and self-aligned top-gate structure have also been explored.[18–21] Although these methods have improved the performance of IGZO TFTs, both mobility and stability of device remains a major challenge. Recently, an effective approach of dual-channel layer heterojunction structure was proposed, wherein the gate dielectric channel layer

†Corresponding author. E-mail: shichensu@scnu.edu.cn
‡Corresponding author. E-mail: wangxh@sdju.edu.cn
§Corresponding author. E-mail: zhuhai5@mail.sysu.edu.cn

© 2025 Chinese Physical Society and IOP Publishing Ltd. All rights, including for text and data mining, AI training, and similar technologies, are reserved.

utilizes high mobility metal–oxide materials, while a high stability material was acted as the composite stacked layer. The combination bilayer enables the attainment of high mobility and high stability TFT devices. Notably, several reports about dual active layer structure such as IGZO/In_2O_3, In_2O_3/ZnSnO:Pr, Ga_2O_3/IGZO, IGZO/ITO, IGZO/IZO, have demonstrated the substantial enhancements of TFT performance, involves the passivation the back channel, confinement the interfacial energy barrier and formation of two-dimensional electron gas (2DEG).[22–26]

In this paper, we fabricated heterojunction composite films of IGZO (In:Ga:Zn=1:1:1, 99.99%) with high indium (In) content and IGZO (In:Ga:Zn=1:2:2, 99.99%) with low In content. Based on the bilayer films, the back gate TFT devices were prepared, and the remarkable performance characteristics were collected. The bilayer IGZO TFTs exhibited the high mobility of 23.5 $cm^2 \cdot V^{-1} \cdot s^{-1}$, high switching ratio of 4.1×10^7, and the steep subthreshold swing of 0.42 V/dec. Compared to single channel TFTs, the field-effect output features of bilayer TFTs were improved obviously, especially the bias stress stability was enhanced dramatically. The excellent transistor characteristics of devices demonstrate the feasibility of our proposed bilayer heterojucntion TFT, which will promote the basic research of IGZO device and accelerate the practical application of transparency IGZO TFT.

2. Experimental details

The amorphous alloy IGZO (In:Ga:Zn=1:1:1) 12-nm, IGZO (In:Ga:Zn=1:2:2) 28-nm films were deposited on heavily doped p-type Si wafers (SiO_2/p^+-Si) with a thermally oxidized layer (100 nm) by magnetron sputtering at room-temperature (RT) with an RF power of 70 W, a vacuum of 5×10^{-4} Pa, and a flow rate of 25 sccm for Ar gas. The active layers were patterned by wet etching (hydrochlo ric acid). The source and drain region was patterned using the ultraviolet photolithography machine (μPG-501). Then the Ti/Au metal electrodes with thickness of 20 nm/100 nm for the source and drain were evaporated by a thermal evaporation technique sequentially. The channel dimensions of TFT devices were control to be W (width) = 40 μm and L (length) = 50 μm. Finally, the devices were annealed at 200 °C, 250 °C, 300 °C, and 350 °C for 40 min in air atmosphere to remove the defects. The electrical output characteristics of TFT devices were carried out by using a semiconductor analyzer (Keithley 4200-SCS) in RT environment. The absorption and transmission spectra of IGZO films were measured via a UV-visible spectrophotometer (Shimadzu UV-2700). The energy band structure of IGZO films was checked by ultra-violet (UV) photoelectron spectroscopy (UPS, Thermo SCIENTIFIC Nexsa) with an HeI UV light source of 21.22 eV. The x-ray photoelectron spectroscopy was used to study the composition and chemical state of IGZO films with an aluminum anode x-ray source of 1486.6 eV (XPS, ESCALAB Xi+, Thermo Fisher). The surface roughness and thickness of samples were explored by atomic force scanning microscopy (AFM, Dimension Fastscan).

3. Results and discussion

As shown in Fig. 1(a), the schematic diagram of the device structure for bilayer IGZO TFT, the channel parameters of W and L are set to be 40 μm and 50 μm respectively. For comparison, the TFT devices with single layer thin-film IGZO (In:Ga:Zn=1:1:1) and (In:Ga:Zn=1:2:2) were growth in the same experimental condition. Moreover, the preparation process and structures of devices are identical to both the single- and dual-layer IGZO TFTs. Figures 1(b)–1(d) illustrate the measurements of AFM surface roughness for the single-layer

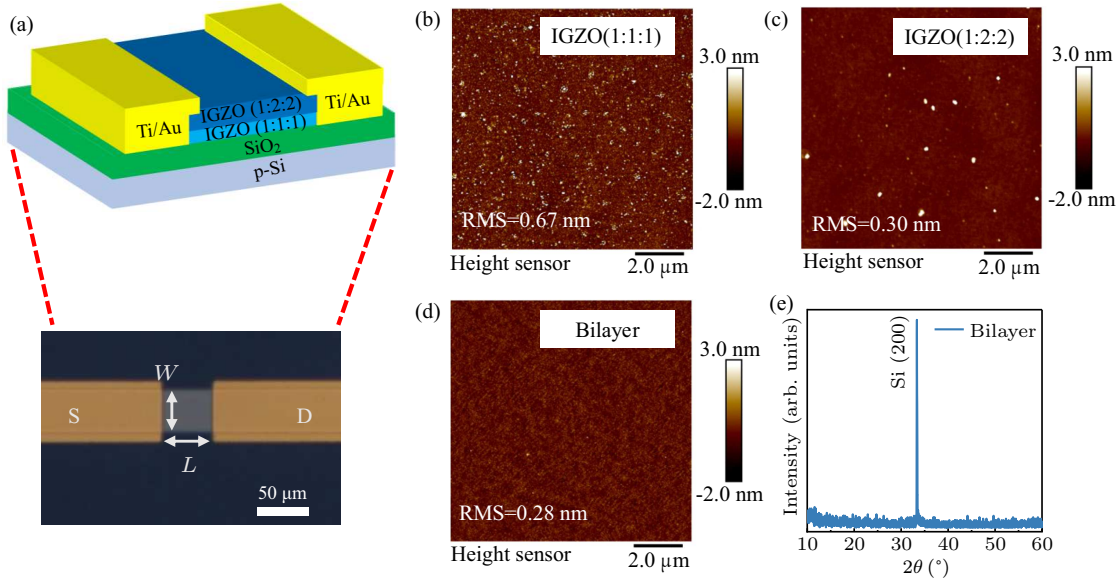


Fig. 1. (a) Schematic structure and optical image of a typical bilayer IGZO TFT. (b) The AFM image of IGZO (In:Ga:Zn=1:1:1) film. (c) The AFM image of IGZO (In:Ga:Zn=1:2:2) film. (d) The AFM image of a bilayer IGZO film. (e) The XRD spectrum of bilayer IGZO film.

and bilayer IGZO films. All three samples give the smooth surface, the values of root-mean square (RMS) are 0.67 nm for IGZO (1:1:1), 0.30 nm for IGZO (1:2:2), and 0.28 nm for bilayer films, respectively. Notably, the smooth surface of these IGZO film will reduce the interface disorder scattering and enhance the field-effect transport capacity of the channel.[22,25] Figure 1(e) presents the XRD pattern of IGZO film, which indicates only typical diffraction peak of Si substrate and no prominent peaks of the metal oxides. Above experimental results confirm that the our prepared IGZO films are amorphous state.

Next, the impact of annealing at various temperatures on the performance of bilayer TFT devices. As depicted in Figs. 2(a)–2(d), the output characteristics curves of annealed devices exhibit favorable transistor behavior as annealing temperature is lower than 350 °C. The device subjected to annealing at 350 °C shows signs of performance degradation, evident from the presence of a Schottky contact in the output characteristic curves as given in Fig. 2(e). The degradation can be attributed to the oxidation of Ti metal electrodes and the formation of barriers at high annealing temperature.

Figure 2(f) illustrates the typical transfer characteristic curves of IGZO TFT devices at $V_{DS} = 1$ V. Several important parameters about TFTs can be extracted from the transfer curves, including subthreshold swing (*SS*), field-effect mobility (μ_{FE}), and switching ratio ($I_{on/off}$). The μ_{FE} is calculated in the linear region of the transfer curve using the formula[27]

$$\mu_{FE} = \frac{L}{C_{ox} W V_{DS}} \left(\frac{dI_{DS}}{dV_{GS}} \right), \tag{1}$$

where C_{ox} indicates the capacitance per unit area of the gate dielectric, which is about 34.5 nF·cm^{-2} for silicon oxide layer (100 nm) in the device. The channel W/L is 40 μm/50 μm, and V_{DS} is fixed at 1 V. The *SS* is defined as[27]

$$SS = \frac{dV_G}{d\lg(I_{DS})}. \tag{2}$$

Using the above equations, the μ_{FE} and *SS* of each TFT devices based on the transfer characteristic curves will be determined. For better investigation of the bilayer IGZO TFT, key performance parameters of the TFTs annealing at various temperatures are compared, as shown in Table 1. The mobility achieves a maximum of 23.5 cm^2·V^{-1}·s^{-1} and sheer *SS* of 0.42 V/dec, indicating the outstanding performance at annealing temperature of 300-°C bilayer IGZO TFT.[28]

Table 1. Parameters μ, *SS*, $I_{on/off}$, and D_{it} of the bilayer IGZO TFT annealing at various temperatures.

Parameters	Unannealed	200 °C	250 °C	300 °C	350 °C
μ (cm^2·V^{-1}·s^{-1})	18.5	19.2	22.8	23.5	3.9
SS (V/dec)	0.83	0.56	0.43	0.42	1.4
$I_{on/off}$ (10^7)	2.7	2.5	4.2	4.1	0.12
D_{it} (10^{12} eV^{-1}·cm^{-2})	2.8	1.8	1.4	1.3	4.9

The interfacial trap density (D_{it}) was calculated based on the following equation:[29]

$$D_{it} = \frac{C_{ox}}{q} \left(\frac{qSS}{K_B T \ln 10} - 1 \right), \tag{3}$$

where C_{ox} is the gate dielectric capacitance per unit area, K_B is the Boltzmann constant, T is the absolute temperature, and q is the unit electron charge. As shown in Table 1, the D_{it} of the 300-°C annealed TFT device is 1.3×10^{12} eV^{-1}·cm^{-2}, which is smaller than that of other devices. These results indicate that the 300-°C annealed TFT devices have a lower interfacial trap density, which ensures that the devices have a lower *SS* and higher field-effect mobility.

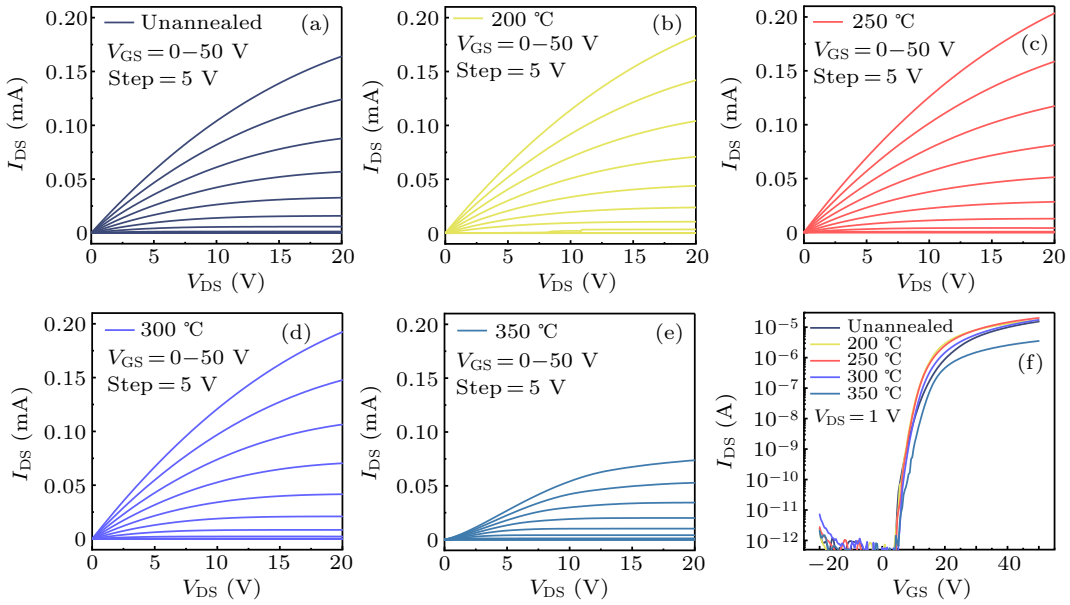


Fig. 2. (a)–(e) Output characteristic curves of bilayer TFT at various annealing temperatures. (f) Transfer characteristics curves of bilayer TFT at various annealing temperatures.

The electrical characterization of single-layer IGZO and bilayer IGZO TFT devices were explored comprehensively. Here, the IGZO (In:Ga:Zn=1:1:1) and (In:Ga:Zn=1:2:2) were referred as IGZO-1 and IGZO-2 for convenience. Figure 3(a) presents the output characteristic curves of the bilayer TFT and IGZO-1 devices annealing at 300 °C respectively, the gate voltages were ranging from V_{GS} = 0–50 V with 5-V increments. Both devices exhibit n-type channel mode operation without current crowding in the linear region, which indicating good Ohmic contact between the metal electrodes and source/drain.

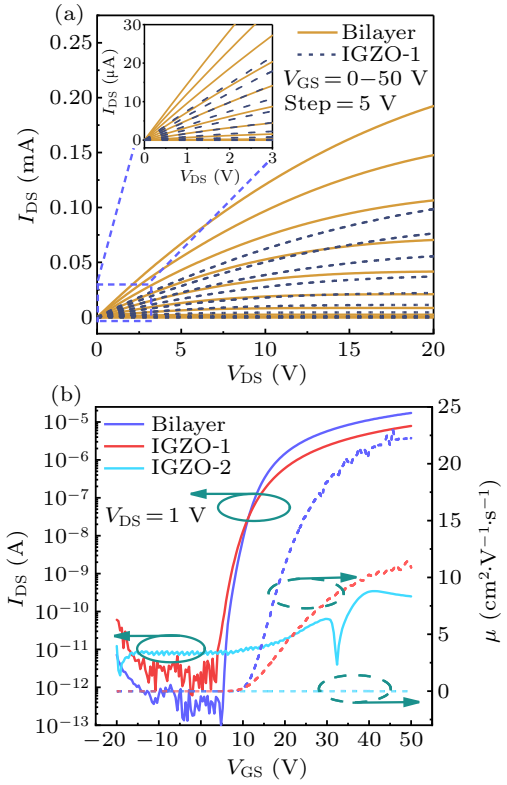


Fig. 3. (a) The output characteristic curves of single layer IGZO-1 and bilayer IGZO TFT, respectively. (b) The typical transfer characteristics and mobility curves of single layer IGZO-1, IGZO-2, and bilayer IGZO TFT.

For single-layer IGZO-2 TFT device, a high turn-on voltage is required due to its large intrinsic resistance in Fig. 3(b), which result in I_{DS} as low as 0.25 nA and cannot be turned on. The value of μ_{FE} is close to zero at V_{DS} = 1 V and V_{GS} = 50 V. For the IGZO-1 TFT device, the *SS* is 1.3 V/dec, while the μ_{FE} reaches a maximum of 11.5 $cm^2 \cdot V^{-1} \cdot s^{-1}$ with the I_{on}/I_{off} of 2.2×10^6. The designed IGZO bilayer TFT device was comprised by a high In content and a low In content IGZO film (12 nm/28 nm), which was anticipated to overcomes the electrical performance limitations of the single layer structure TFT device.

In contrast, the transfer characteristic curve of bilayer IGZO TFT exhibits a μ_{FE} of 23.5 $cm^2 \cdot V^{-1} \cdot s^{-1}$, the *SS* of 0.42 V/dec, the I_{on}/I_{off} current ratio of 4.1×10^7. Remarkable, the field-effect mobility μ_{FE} of the bilayer TFT has been significantly increased from 11.5 $cm^2 \cdot V^{-1} \cdot s^{-1}$ to 23.5 $cm^2 \cdot V^{-1} \cdot s^{-1}$ compared to single layer devices. Moreover, the performance of bilayer IGZO TFT displays superior electrical characteristics not only better than single layer IGZO-1 but also than the IGZO-2 devices. Consequently, the output properties of bilayer IGZO TFT devices at RT is optimized through the construction of the composite two IGZO layers with different In-contents. Table 2 represents the comparisons of electrical performance of TFT device with bilayer structure reported in recent years. It is noteworthy that a lower mobility IGZO layer with a lower indium component was proposed and used as an active layer in our designed device. Without introducing an active layer with a higher content of In, the device's performance closely matches or even surpasses that of a bilayer TFT device utilizing high mobility materials.

To gain the underlying mechanism of the interface for bilayer IGZO films TFT, an analysis of the energy band structures of IGZO-1 and IGZO-2 films were conducted. Initially, the measurement of UV-visible absorption and transmission spectroscopy for samples were performed. We fitted the optical band gaps (E_g) of the two films separately using the following equation:[36]

$$(\alpha h\nu)^2 = h\nu - E_g, \tag{4}$$

here, α represents the absorption coefficient, h is the Planck constant, and ν denotes the incident photon frequency.

Table 2. Electrical performance parameters of bilayer metal–oxide TFTs reported in recent years.

Channel layer	Fabrication temperature (°C)	μ ($cm^2 \cdot V^{-1} \cdot s^{-1}$)	$I_{on/off}$	*SS* (V/dec)	Year	References
IGZO/In_2O_3	230	7.63	7.18×10^7	1.52	2024	[30]
IGZO/ITZO	450	21.27	$\sim 10^7$	0.51	2014	[31]
IGZO/ITZO	450	20.24	6×10^8	0.42	2018	[32]
IGZO/IZO	400	8.3	1.67×10^7	1.43	2022	[26]
IGZO/In_2O_3	400	14.5	$\sim 10^6$	–	2019	[33]
IGZO/In_2O_3	350	47.9	10^9	0.08	2023	[22]
Ga_2O_3/IGZO	170	15.8	1.2×10^7	0.6	2022	[23]
IGZO/ZnON	350	24.75	–	0.32	2020	[34]
IGO/In_2O_3	300	3.21	$\sim 10^6$	1.61	2021	[35]
IGZO/IGZO	300	23.5	4.1×10^7	0.42	2025	this work

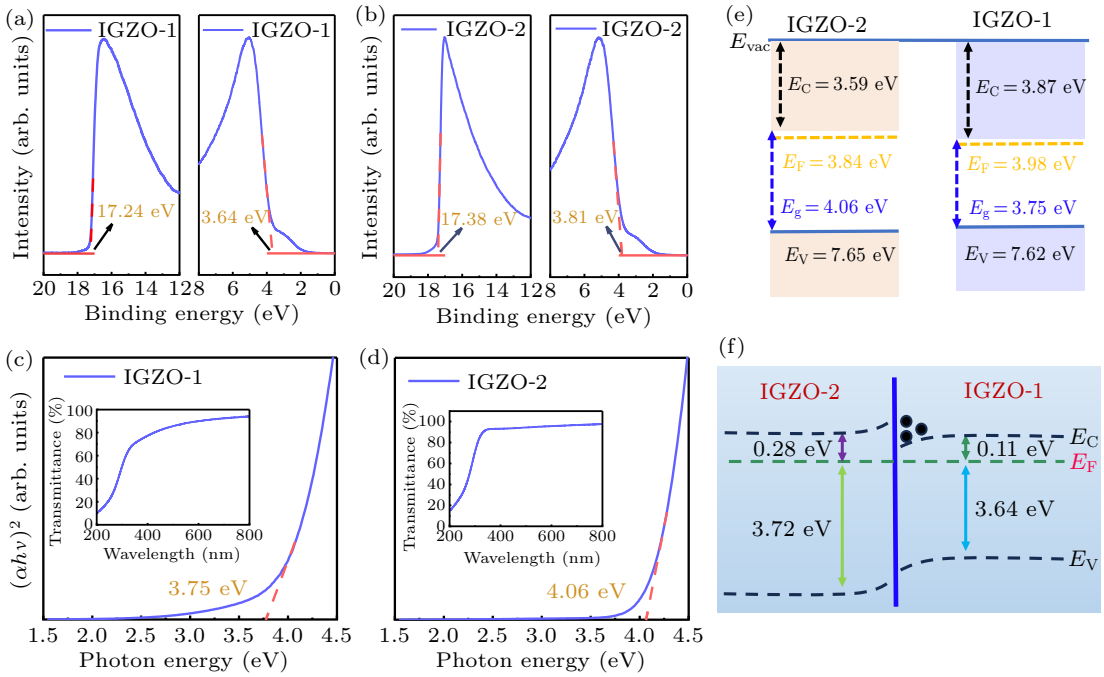


Fig. 4. (a)–(b) The UPS spectrum of IGZO-1 and IGZO-2 film. (c)–(d) The UV-vis absorption and transmission spectra of IGZO-1 and IGZO-2 films. The optical band gap of samples can be obtained from the spectra. (e) Energy band structure of IGZO-1 and IGZO-2 films before matching. (f) Energy band structure and electron distribution in heterojunction after formation.

Figures 4(a) and 4(b) represent the ultraviolet photoelectron spectroscopy (UPS) analysis for the IGZO thin films. Based on the figure of work function spectrum, the secondary electron cut-off energy ($E_{\text{cut-off}}$) of IGZO-1 and IGZO-2 are determined to be 17.24 eV and 17.38 eV, respectively. The energy of UV light source in UPS instrument is 21.22 eV. Subtracting this 21.22 eV from the $E_{\text{cut-off}}$, results in the figure of Fermi energy level (E_{F}) of 3.98 eV for IGZO-1 and 3.84 eV for IGZO-2. Consider the valence band spectrum of IGZO, the relative Fermi energy levels of valence band maxima (E_{V}) are determined to be 3.64 eV for IGZO-1 and 3.81 eV for IGZO-2.

As illustrated in Figs. 4(c) and 4(d), the absorption–transmission spectra of IGZO-1 and IGZO-2 give an excellent transmittance with an average transmittance of around 90% for wavelengths above 400 nm. The E_{g} of IGZO-1 and IGZO-2 are 3.75 eV and 4.06 eV, respectively.[37] The variance in bandgap between IGZO-1 and IGZO-2 can be attributed to the predominant use of indium in furnishing electrons within IGZO films. Higher indium content results in increased electron provision and subsequently leads to a smaller bandgap.[38] This remarkable transparency, combined with a broad optical band gap, makes IGZO films less susceptible to light interference, a crucial characteristic for maintaining the light reliability of IGZO TFT devices during their operation. Applying the formula conduction band minimum $(E_{\text{C}}) = E_{\text{V}} - E_{\text{g}}$, hence the E_{C} for IGZO-1 and IGZO-2 can be extracted to be 3.59 eV and 3.87 eV.

Figure 4(e) displays the energy band structures of two IGZO films and the vacuum energy level (E_{vac}). It illustrates that Fermi energy level of IGZO-1 is lower than that of IGZO-2. During the heterojunction matching, the alignment of Fermi energy levels at interface causes the $E_{\text{c}}/E_{\text{v}}$ in IGZO-2 to bend upwards while those in IGZO-1 bend downwards due to the maintenance of thermal equilibrium, as depicted in Fig. 4(f). Consequently, the electrons in E_{c} will migrate from IGZO-2 into IGZO-1, resulting in electrons accumulation and confinement in IGZO-1.[39] The potential energy barrier (0.17 eV) similar to the formation of two-dimensional electron gas (2DEG) in heterojunction, which can enhance the electron mobility effectively.[22–25,40]

For investigate the impact of bilayer structure on the stability of electrical characteristics for IGZO TFT devices, we performed the positive gate bias stress stability (PBS) and negative gate bias stress (NBS) stability tests. The TFT devices were subjected to a bias voltage of ±20 V for a duration of 3600 s in dark environment at RT. Figures 5(a) and 5(b) illustrate the variation of transfer characteristic curves for single-layer IGZO-1 TFTs under PBS and NBS. It is evident that the V_{th} of single-layer device experiences significant changing after bias stress (3600 s), with a positive shifting of 4.1 V under PBS and a negative shifting of −3.4 V under NBS. Furthermore, the variation of the transfer characteristic curves of bilayer IGZO TFT under PBS and NBS were also explored, as shown in Figs. 5(c)–5(f). In contrast with the single-layer devices, the bilayer device exhibits excellent electrical stability under the same conditions, which shows a smaller degradation in V_{th}. It is noted that the unannealed bilayer device experience the variations of 2.1 V under PBS and −1.3 V under NBS, the bilayer device at annealing temperature of 300 °C exhibits only 1.5 V under PBS and −1.1 V under NBS.

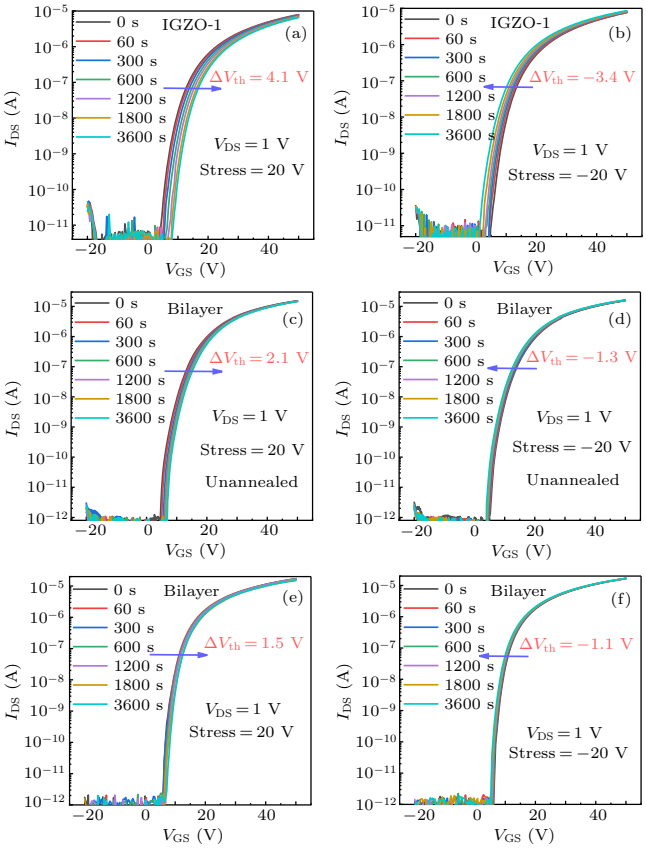


Fig. 5. (a) The PBS test of a single-layer IGZO-1 TFT at annealing temperature of 300 °C, (b) the NBS test of a single-layer IGZO-1 TFT at annealing temperature of 300 °C, (c) the PBS test of unannealed bilayer IGZO TFT, and (d) the NBS test of unannealed bilayer IGZO TFT, (e) the PBS test of bilayer IGZO TFT at annealing temperature of 300 °C, and (f) the NBS test of bilayer IGZO TFT at annealing temperature of 300 °C.

Figures 6(a)–6(c) illustrate the variations in μ, SS, and ΔV_{th} as functions of stress time under a bias stress of 20 V. The electrical parameters (μ, SS, and ΔV_{th}) of all three IGZO TFT devices exhibit an overall degradation trend with prolonged stress time. However, regardless of the annealing treatment, the bilayer IGZO TFT demonstrates significantly smaller variations in electrical characteristics compared to single-layer devices. Above results demonstrate that the bilayer structure significantly enhances the stability of IGZO TFT devices. The enhancement of stability can be attributed to the incorporation of IGZO-2 with low In content, which was acted as a passivation layer effectively. The top IGZO-2 layer can compensate the suspended bond and neutralize the interface state of IGZO-1, on the other hand it isolates water vapor in the air for TFTs. As a result, the transport channel of the underlying IGZO-1 can be no longer exposed to the air. Hence, the electrical characteristics and stability of the bilayer TFT devices were improved distinctly.

In order to explore the intrinsic mechanism of the bilayer IGZO TFTs, the evolution of chemical state in bilayer IGZO films was investigated using XPS technique. The bilayer IGZO film composition was IGZO-1/IGZO-2=12 nm/28 nm, and the XPS analysis was performed on the IGZO-2 surface. The measured results of XPS are presented in Figs. 7(a) and 7(b), where the peak of O 1s orbital can be divided into three sub-peaks. The sub-peak that located at 529.9±0.2 eV corresponds to the chemical bonding between oxygen and metal (M–O) in the film. Moreover, the peak at 531.1±0.2 eV is associated with oxygen vacancies (V_o) within the film, while the highest binding energy peak at 532.0±0.2 eV can be attributed to specific chemisorption feature of the film (M–OH).[14,21] Based on Gaussian fitting, the contribution of V_o peak area in unannealed bilayer IGZO film is 26.4%. In contrast, the contribution of V_o was decreased to 22.5% in bilayer IGZO film at annealing temperature of 300 °C, as given in Fig. 7(b). In amorphous metal oxide materials, oxygen vacancies typically act as electron donors and give rise to high electron concentration. Several reports have indicated that the density of V_o in the active layer is correlated with the stability of IGZO TFT devices.[41,42] Specifically, the lower V_o density will enhance bias stability of device strongly. For the bilayer structure, the annealing method can effectively reduce the oxygen vacancy density, which promotes bias stability.

We fabricated devices with varying channel lengths to investigate the uniformity of the electrical characteristics in the bilayer TFT devices. Figures 8(a)–8(g) illustrates the output characteristic curves of these devices with different channel lengths, revealing no current crowding in the linear region, indicating robust ohmic contacts. The consistent transfer characteristics of the device in the range of $L = 30$ μm–360 μm,

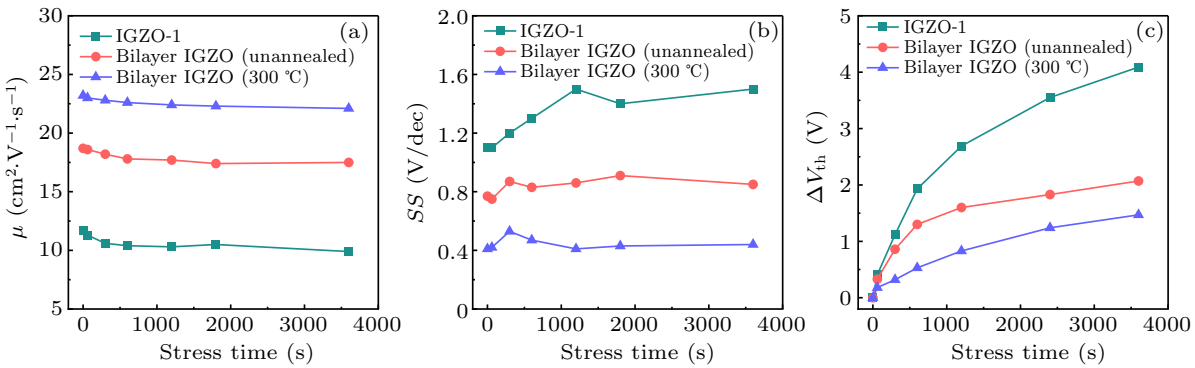


Fig. 6. Time-dependent variations in (a) μ, (b) SS, and (c) ΔV_{th} under 20-V bias stress for single-layer IGZO-1, unannealed bilayer IGZO, and 300 °C-annealed bilayer IGZO TFTs.

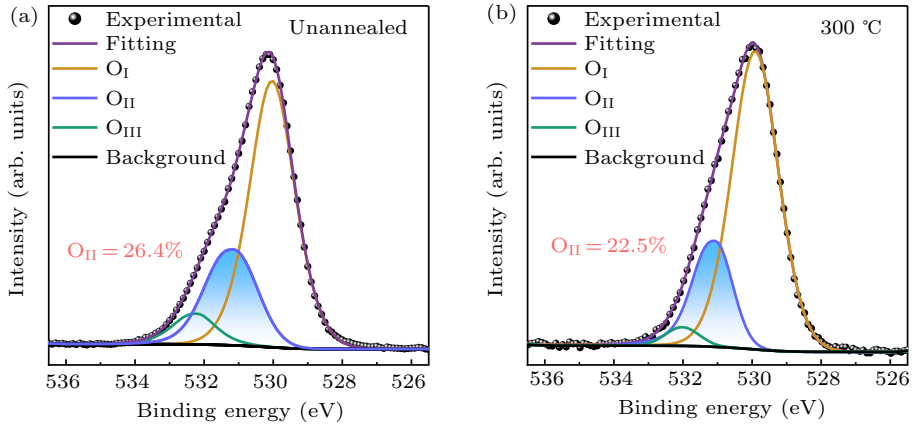


Fig. 7. (a) The XPS spectrum of unannealed bilayer IGZO film. (b) The XPS spectrum of bilayer IGZO films at annealing temperature of 300 °C.

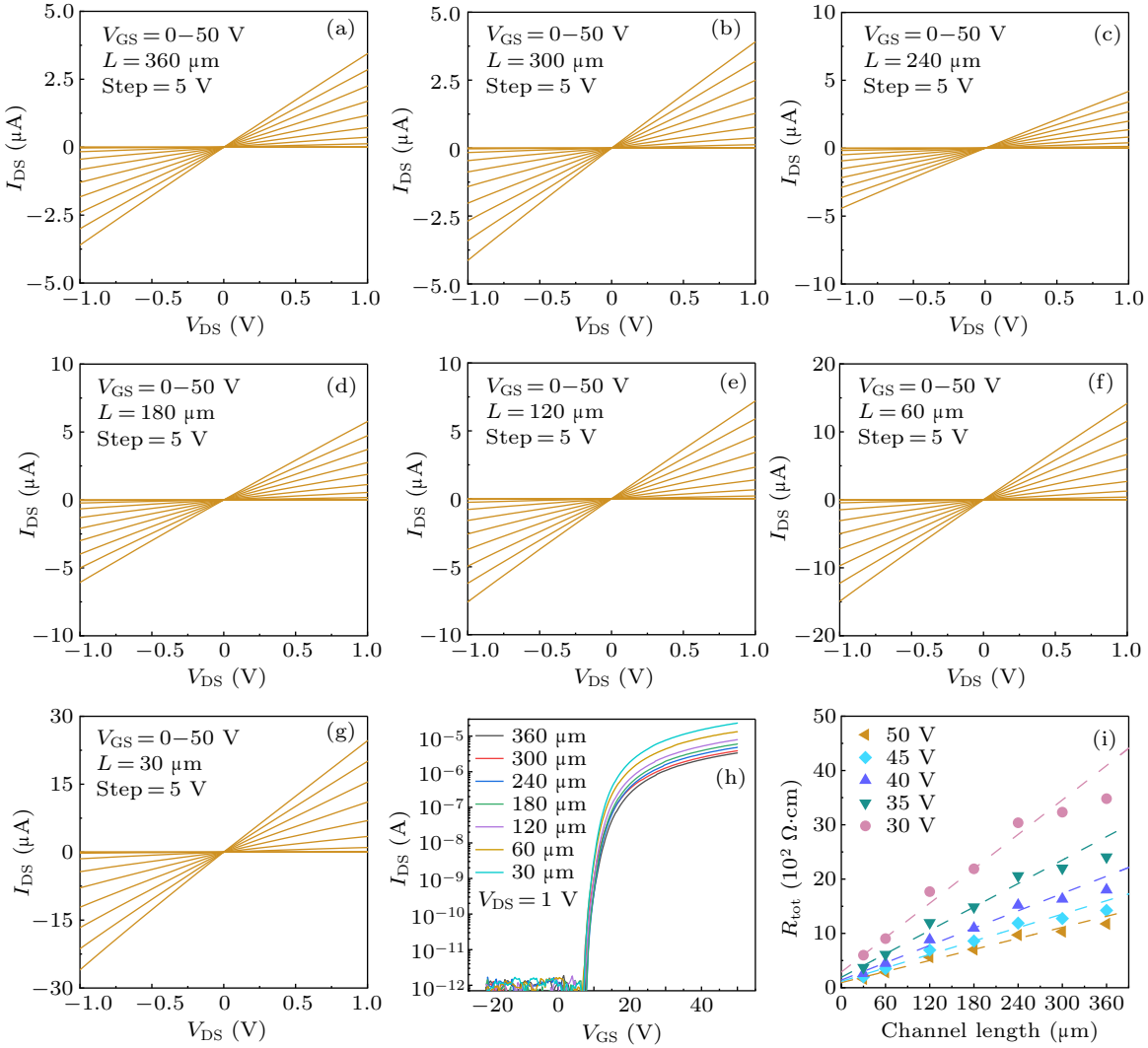


Fig. 8. (a)–(g) Output characteristic curves of bilayer TFT at $W = 50$ μm of different L. (h) Transfer characteristic curves of bilayer TFT at $W = 50$ μm of different L. (i) Total resistance as a function of varying L.

shown in Fig. 8(h), showcase the downscaling capability of the bilayer TFT devices. The contact resistance was fitted according to the transfer-length method (TLM) with the following equation:[27]

$$R_{tot} = \frac{V_{DS}}{I_{DS}} = r_{ch}L + R_c, \tag{5}$$

where R_{tot}, r_{ch}, and R_c are normalized product of the total resistance and W, channel resistance, and normalized product of the contact resistance and W, respectively. Based on the linear fitting and extracting the intercept value in Fig. 8(i), the R_c magnitude was calculated as 47 Ω·cm at $V_{GS} = 50$ V. The TLM method confirms the small R_c.

4. Conclusions

In summary, the excellence electrical properties of bilayer IGZO TFTs by a composite structure that consisting of two films with different In content concentrations were demonstrated. The design bilayer IGZO TFT devices were fabricated with back gate at RT. Compared to the single-layer TFT, the bilayer structure device exhibit remarkable electrical characteristics. The field-effect mobility μ_{FE} was increased to 23.5 $cm^2 \cdot V^{-1} \cdot s^{-1}$, the *SS* reduced to 0.42 V/dec, and the $I_{on/off}$ improved to 4.1×10^7. Furthermore, the V_{th} of TFTs exhibited extremely faint variations under PBS and NBS tests, which demonstrates the excellent bias stability. The incorporation of low In content IGZO film in the bilayer device was served as a passivation layer, which effectively reduced the oxygen vacancy and prevent water vapor in the environment from the transport channel. The potential barrier at heterojunction interface was illustrated by UPS, which resulting in high carrier mobility for TFT device. Our design approach provides a valuable reference for further research and practical applications of IGZO TFT devices and promotes a referable method for foundation research of IGZO materials.

Acknowledgements

Project supported by the National Natural Science Foundation of China (Grant Nos. U22A2073 and 62474197) and the Basic and Applied Basic Research Foundation of Guangdong Province, China (Grant Nos. 2024A1515011536 and 2025A04J7142).

References

[1] Geng D, Wang K, Li L, Myny K, Nathan A, Jang J, Kuo Y and Liu M 2023 *Nat. Electron.* **6** 963
[2] Nomura K, Ohta H, Takagi A, Kamiya T, Hirano M and Hosono H 2004 *Nature* **432** 488
[3] Kang Y, Lee W, Kim J, Keum K, Kang S H, Jo J W, Park S K and Kim Y H 2021 *Mater. Res. Bull.* **139** 111252
[4] Li Z Y, Song S M, Wang W X, Gong J H, Tong Y, Dai M J, Lin S S, Yang T L and Sun H 2022 *Nanotechnology* **34** 025702
[5] Chen F, Zhang M, Wan Y, Xu X, Wong M and Kwok Hoi S 2023 *J. Semicond.* **44** 091620
[6] Xiong W, Huo J Y, Wu X H, Liu W J, Zhang D W and Ding S J 2023 *Chin. Phys. B* **32** 018503
[7] Zhu Y, He Y, Jiang S, Zhu L, Chen C and Wan Q 2021 *J. Semicond.* **42** 031101
[8] Ito M, Kon M, Miyazaki C, Ikeda N, Ishizaki M, Matsubara R, Ugajin Y and Sekine N 2008 *Phys. Status Solidi A* **205** 1885
[9] Tang H, Li Y, Sokolovskij R, Sacco L, Zheng H, Ye H, Yu H, Fan X, Tian H, Ren T L and Zhang G 2019 *ACS Appl. Mater. Interfaces* **11** 40850
[10] Honda W, Harada S, Ishida S, Arie T, Akita S and Takei K 2015 *Adv. Mater.* **27** 4674
[11] Liu Y, Zhou H L, Cheng R, Yu W J, Huang Y and Duan X F 2014 *Nano Lett.* **14** 1413
[12] Zhang M N, Shao Y, Wang X L, Wu X, Liu W J and Ding S J 2020 *Chin. Phys. B* **29** 078503
[13] Song S, Liang H, Huo W, Zhang G, Zhang Y, Wang J and Mei Z 2024 *Chin. Phys. Lett.* **41** 068501
[14] Abliz A 2021 *IEEE Trans. Electron Dev.* **68** 3379
[15] Abliz A, Gao Q G, Wan D, Liu X Q, Xu L, Liu C S, Jiang C Z, Li X F, Chen H P, Guo T L, Li J C and Liao L 2017 *ACS Appl. Mater. Interfaces* **9** 10798
[16] Liu W S, Hsu C H, Jiang Y, Lai Y C and Kuo H C 2022 *Membranes (Basel)* **12** 49
[17] Abliz A 2020 *J. Alloys Compd.* **831** 154694
[18] Hong H Y M, Yi D J, Moon Y K, Son K S, Lim J H, Jeong K and Chung K B 2024 *IEEE Trans. Electron Dev.* **71** 1097
[19] Peng C, Huang H X, Xu M, Chen L L, Li X F and Zhang J H 2022 *Nanomaterials* **12** 4021
[20] Li J, Zhang Y, Wang J, Yang H, Zhou X, Chan M, Wang X, Lu L and Zhang S 2022 *IEEE Electron Dev. Lett.* **43** 729
[21] Peng H, Chang B, Fu H, Yang H, Zhang Y, Zhou X, Lu L and Zhang S 2020 *IEEE Trans. Electron Dev.* **67** 1619
[22] Guo M, Ou H, Xie D Y, Zhu Q J, Wang M Y, Liang L Y, Liu F J, Ning C, Cao H T, Yuan G C, Lu X B and Liu C 2023 *Adv. Electron. Mater.* **9** 2201184
[23] Ji X, Yuan Y, Yin X, Yan S, Xin Q and Song A 2022 *IEEE Trans. Electron Dev.* **69** 6783
[24] Park C Y, Jeon S P, Park J B, Park H B, Kim D H, Yang S H, Kim G, Jo J W, Oh M S, Kim M, Kim Y H and Park S K 2023 *Ceram. Int.* **49** 5905
[25] Zhu Q, Huang Y, Wu J, Guo M, Ou H, Liu B, Lu X, Chen J, Liang X, Wu Q and Liu C 2024 *IEEE Electron Dev. Lett.* **45** 845
[26] Sun Q J, Wu J, Zhang M, Yuan Y, Gao X, Wang S D, Tang Z, Kuo C C and Yan Y 2022 *Phys. Status Solidi A* **219** 2200311
[27] Fortunato E, Barquinha P and Martins R 2012 *Adv Mater* **24** 2945
[28] Wang C, Lu W, Li F, Luo Q and Ma F 2022 *Chin. Phys. B* **31** 096101
[29] Abliz A, Wang J, Xu L, Wan D, Liao L, Ye C, Liu C, Jiang C, Chen H and Guo T 2016 *Appl. Phys. Lett.* **108** 213501
[30] Zhang Q, Xia G, Li H, Sun Q, Gong H and Wang S 2024 *Nanotechnology* **35** 125202
[31] Rim Y S, Chen H, Kou X, Duan H S, Zhou H, Cai M, Kim H J and Yang Y 2014 *Adv. Mater.* **26** 4273
[32] Lee M, Jo J W, Kim Y J, Choi S, Kwon S M, Jeon S P, Facchetti A, Kim Y H and Park S K 2018 *Adv. Mater.* **30** 1804120
[33] Liang K, Wang Y, Shao S, Luo M, Pecunia V, Shao L, Zhao J, Chen Z, Mo L and Cui Z 2019 *J. Mater. Chem. C* **7** 6169
[34] Kim Y S, Lee H M, Lim J H and Park J S 2020 *Appl. Phys. Lett.* **117** 143505
[35] He F, Wang Y, Yuan H, Lin Z, Su J, Zhang J, Chang J and Hao Y 2021 *Ceram. Int.* **47** 35029
[36] Tauc J, Grigorovici R and Vancu A 1966 *Phys. Status Solidi B* **15** 627
[37] Wen P, Peng C, Chen Z, Ding X, Chen F-H, Yan G, Xu L, Wang D, Sun X, Chen L, Li J, Li X and Zhang J 2024 *Appl. Phys. Lett.* **124** 133501
[38] Swallow J E N, Palgrave R G, Murgatroyd P A E, Regoutz A, Lorenz M, Hassa A, Grundmann M, von Wenckstern H, Varley J B and Veal T D 2021 *ACS Appl. Mater. Interfaces* **13** 2807
[39] Ma X, Wang Z, Qin Q, Chen J, Liu X, Zou F, Xu Z, Chen W, Li G, Li Y, Zhai T and Li L 2025 *Adv. Mater.* **37** 2500572
[40] Cho M H, Choi C H, Seul H J, Cho H C and Jeong J K 2021 *ACS Appl. Mater. Interfaces* **13** 16628
[41] Zheng L L, Ma Q, Wang Y H, Liu W J, Ding S J and Zhang D W 2016 *IEEE Electron Dev. Lett.* **37** 743
[42] Guo J, Zhang D, Wang M and Wang H 2021 *Chin. Phys. B* **30** 118102